Monthly Notices
of the
ROYAL ASTRONOMICAL SOCIETY

MNRAS **460,** 1934–1945 (2016)
Advance Access publication 2016 May 5

doi:10.1093/mnras/stw1061

Matching dust emission structures and magnetic field in high-latitude cloud L1642: comparing *Herschel* and *Planck* maps⋆

J. Malinen,[1]† L. Montier,[2,3] J. Montillaud,[4] M. Juvela,[5] I. Ristorcelli,[2,3] S. E. Clark,[6] O. Berné,[2,3] J.-Ph. Bernard,[2,3] V.-M. Pelkonen[4] and D. C. Collins[1]

[1]*Department of Physics, Florida State University, Tallahassee, FL 32306, USA*
[2]*Université de Toulouse, UPS-OMP, IRAP, F-31028 Toulouse cedex 4, France*
[3]*CNRS, IRAP, 9 Av. colonel Roche, BP 44346, F-31028 Toulouse cedex 4, France*
[4]*Institut Utinam, CNRS UMR 6213, OSU THETA, Université de Franche-Comté, 41bis avenue de l'Observatoire, F-25000 Besançon, France*
[5]*University of Helsinki, PO Box 64, FI-00014 Helsinki, Finland*
[6]*Department of Astronomy, Columbia University, New York, NY 10027, USA*

Accepted 2016 May 3. Received 2016 April 29; in original form 2015 December 10

ABSTRACT

The nearby cloud L1642 is one of only two known very high latitude ($|b| > 30$ deg) clouds actively forming stars. It is a rare example of star formation in isolated conditions, and can reveal important details of star formation in general, e.g. of the effect of magnetic fields. We compare *Herschel* dust emission structures and magnetic field orientation revealed by *Planck* polarization maps in L1642. The high-resolution (∼20 arcsec) *Herschel* data reveal a complex structure including a dense, compressed central clump, and low-density striations. The *Planck* polarization data (at 10 arcmin resolution) reveal an ordered magnetic field pervading the cloud and aligned with the surrounding striations. There is a complex interplay between the cloud structure and large-scale magnetic field. This suggests that the magnetic field is closely linked to the formation and evolution of the cloud. CO rotational emission confirms that the striations are connected with the main clumps and likely to contain material either falling into or flowing out of the clumps. There is a clear transition from aligned to perpendicular structures approximately at a column density of $N_{\rm H} = 1.6 \times 10^{21}$ cm^{-2}. Comparing the *Herschel* maps with the *Planck* polarization maps shows the close connection between the magnetic field and cloud structure even in the finest details of the cloud.

Key words: polarization – ISM: clouds – ISM: magnetic fields – submillimetre: ISM.

1 INTRODUCTION

The major physical processes involved in molecular cloud and star formation are gravitation, turbulence, magnetic fields, and thermal pressure, but the full picture is not clear, especially regarding the relative importance of turbulence and magnetic fields (e.g. Bergin & Tafalla 2007; McKee & Ostriker 2007; Crutcher 2012; André et al. 2014). The Galactic magnetic field covers our whole Galaxy and takes part in the dynamics of the interstellar medium (ISM) and in the different phases of the star formation process, from molecular clouds to filaments and cores where stars are born.

Magnetic fields can be studied using several methods, including Zeeman splitting of spectral lines and polarization of starlight or thermal dust emission. In this paper, we use the last method, polarized dust emission. Because dust grains are not spherical, their radiation is polarized along the main grain axis. When grains are aligned with a magnetic field, the observed thermal radiation is linearly polarized (e.g. Davis & Greenstein 1951; Vaillancourt 2007). The grains align with their long axis perpendicular to the magnetic field orientation. Therefore, if the polarization vectors are rotated by 90 deg, the dust observations reveal the magnetic field orientation in the plane of the sky (POS).

Ground-based observations of polarized starlight in diffuse areas (e.g. Myers & Goodman 1991; Pereyra & Magalhães 2004) and dust emission in dense areas (e.g. Ward-Thompson et al. 2000; Crutcher et al. 2004) have shown that the POS magnetic field lines are linked to the cloud structures.

Recently, *Planck* satellite has observed the whole sky in submm-mm wavelengths, including the polarization with high enough sensitivity to map magnetic fields both in dense and diffuse areas (Planck Collaboration I 2014). Planck Collaboration XIX (2015) presented an overview of the *Planck* polarization data, and reported a systematic decrease of the polarization fraction with increasing column density. Planck Collaboration XX (2015) compared the polarization

⋆ *Herschel* is an ESA space observatory with science instruments Q14 provided by European-led Principal Investigator consortia and with important participation from NASA.

† E-mail: johanna.malinen@alumni.helsinki.fi

observations with magnetohydrodynamical simulations, and came to the same conclusion that the polarization fraction is highest in the most diffuse areas. Planck Collaboration XXXII (2016) studied large, localized filamentary structures, which they called 'ridges', in the Galaxy having hydrogen column densities ($N_{\rm H}$) between 10^{20} and 10^{22} cm^{-2}, and found that these structures can be seen also in the polarization data (Stokes Q and U maps). The structures are usually aligned with the magnetic field, especially at lower column densities. Planck Collaboration XXXIII (2016) analysed and modelled three filaments in more detail. Planck Collaboration XXXV (2016) made a quantitative analysis of the orientation of the magnetic field and column density structures in 10 nearby clouds, finding that the relative orientation is likely to change from preferentially parallel or without a preferred orientation to perpendicular with increasing column density, the change occurring at $N_{\rm H} \sim 10^{21.7}$ cm^{-2}.

Several observational studies have revealed more details in the diffuse ISM structure. Goldsmith et al. (2008) and Palmeirim et al. (2013) compared earlier magnetic field observations with CO data and *Herschel* dust emission maps, respectively, concluding that striations in the diffuse ISM tend to be parallel to magnetic field lines and perpendicular to denser filaments. Clark, Peek & Putman (2014) and Clark et al. (2015) found linear, several degrees long structures, 'fibers', at high Galactic latitude in neutral hydrogen (H I) maps at 4 arcmin resolution. They compared H I to polarized starlight and *Planck* dust polarization, and concluded that the 'fibers' are closely aligned with magnetic fields.

As observations reveal more and more details of elongated structures at different size scales of the ISM and molecular clouds, the nomenclature is still developing and sometimes ambiguous between different subfields. Here, we use the following definitions for different types of structures, most of them elongated or 'filamentary'. By 'filament' we mean an elongated, medium-low column density structure (approximately at $N_{\rm H} > 2 \times 10^{21}$ cm^{-2}, but this is not a strict limit) linked to low-mass star-forming regions. By 'fiber' we mean elongated sub-structure of filaments (as used in André et al. 2014). By 'striation' we mean any low column density structure (approximately at $N_{\rm H} < 2 \times 10^{21}$ cm^{-2}) which is either linear or curving, and either at diffuse areas or connected to denser filaments or other structures. By 'blob' we mean an irregular structure of relatively dense matter which is more round than filamentary.

Malinen et al. (2014) presented *Herschel* dust emission maps of molecular cloud L1642, which showed clear striations in the diffuse matter surrounding the cloud. L1642 is one of only two high-latitude ($|b| > 30^\circ$) clouds confirmed to have active star formation. The high galactic latitude ($-36\overset{\circ}{.}55$) with very low line-of-sight contamination, small distance (140 pc or less; Hearty et al. 2000; Schlafly et al. 2014), and relatively low column density make the cloud a good object for studying low-mass star formation (see McGehee 2008; Malinen et al. 2014).

Our aim in this paper is to study the magnetic fields revealed by *Planck* dust polarization maps and compare them to the striations and other structures shown in the higher resolution *Herschel* maps of L1642. Previous *Planck* papers have used the polarization maps only in combination with the *Planck* intensity maps, at best at ∼5 arcmin resolution, but usually convolved to lower resolution (∼10 arcmin). We will show that the *Planck* magnetic field maps can be very useful even when compared to higher resolution intensity maps, like *Herschel* at ∼20–40 arcsec resolution.

The contents of this paper are the following: we present the observations and data processing in Section 2, and methods in Section 3. We analyse the cloud structure using *Herschel* maps and compare it to the magnetic fields and kinematic data in Section 4. We discuss the implications of the results in Section 5 and draw our conclusions in Section 6.

2 OBSERVATIONS AND DATA PROCESSING

2.1 *Herschel*

L1642 (G210.90−36.55) was observed by *Herschel* (Pilbratt et al. 2010) as part of the Galactic Cold Cores project (Juvela et al. 2012). The data were presented and described in Malinen et al. (2014). Here, we use *Herschel* 250 μm dust emission map, which shows striations of the diffuse material surrounding the cloud, and hydrogen column density map for separating dense and diffuse areas. We have calculated the column density $N_{\rm H}$ by assuming that emissivity spectral index β is 1.8, and dust opacity κ is 0.1 cm^2/g $(\nu/1000\ {\rm GHz})^\beta$, which is assumed to be valid in high-density environments (Hildebrand 1983; Beckwith et al. 1990).

2.2 *Planck*

Planck satellite has observed linear polarization of the whole sky at seven bands between 30 and 353 GHz (Planck Collaboration I 2014). The data are available through the Planck Legacy Archive.[1] We use the polarized dust signal measured by the *Planck*-HFI 353 GHz channel, where the signal-to-noise ratio (S/N) of the dust emission is maximum, as a tracer of the magnetic field (B). The *Planck* observations provide Stokes I, Q, and U parameter maps. The total polarized intensity P, polarization fraction p, polarization angle ψ, and POS magnetic field orientation angle $\theta_{\rm B}$ can be derived from the Stokes parameters using the equations

$$P = \sqrt{Q^2 + U^2}, \tag{1}$$

$$p = P/I, \tag{2}$$

$$\psi = 0.5 \arctan(-U, Q), \tag{3}$$

$$\theta_{\rm B} = \psi + \pi/2. \tag{4}$$

In equation (3), arctan $(-U, Q)$ gives the angle arctan$(-U/Q)$ in the correct quadrant, and the minus sign converts the *Planck* data from `Healpix` to IAU convention, where the polarization angle is counted positively from the Galactic north to the east. See, e.g., Planck Collaboration XIX (2015) for more details.

Since our object, L1642, is located at high latitude, *Planck* data have to be processed further to increase the S/N of the polarization quantities and to avoid any bias issues, as recommended by Montier et al. (2015a). Hence, the *Planck* maps at 353 GHz have been smoothed to 10 arcmin in order to reach an S/N > 4 in a region of a 30 arcmin radius centred on the cloud. Moreover, the modified asymptotic estimator (hereafter MAS; Plaszczynski et al. 2014) has been chosen to provide a robust estimate of the polarization fraction, $p_{\rm MAS}$, as described in Montier et al. (2015b). With this setup, the uncertainty of the polarization angle remains below 5° in the cloud and in most of the surrounding areas.

For the analysis of the regularity of the B field, we will also use the polarization angle dispersion function, as defined in Planck Collaboration XIX (2015) with the following quantity:

$$S(\boldsymbol{x}, \delta) = \left(\frac{1}{N} \sum_{i=1}^{N} (\Delta\psi_{xi})^2 \right)^{1/2} \tag{5}$$

[1] http://www.cosmos.esa.int/web/planck/pla

where $\Delta\psi_{xi} = \psi(\boldsymbol{x}) - \psi(\boldsymbol{x} + \boldsymbol{\delta}_i)$ is the angle difference between $\psi(\boldsymbol{x})$, the polarization angle at a given sky position $\boldsymbol{x}$ (the central pixel), and $\psi(\boldsymbol{x} + \boldsymbol{\delta}_i)$, the polarization angle at a sky position displaced from the centre by $\boldsymbol{\delta}_i$. The average is computed over an annulus of radius $\delta = |\boldsymbol{\delta}|$ and width $\Delta\delta$. We use value 3.4 arcmin for both radius and width.

2.3 CO rotational emission

We examine the dynamics of the cloud with the CO observations of Russeil et al. (2003), used also in Malinen et al. (2014). The Swedish-ESO Submillimetre Telescope (SEST) radio telescope mapped L1642 in the $J = 1$–0 and $J = 2$–1 transitions of ^{12}CO, ^{13}CO, and C^{18}O. The half-power beam widths of the data are 45 arcsec for $J = 1$–0 and 23 arcsec for $J = 2$–1. The grid has 3 arcmin spacing. Typical noise levels are $\Delta T_{\rm rms} = 0.06$ K for C^{18}O(2–1) and $\sim$0.15 K for other transitions.

3 METHODS

3.1 Line integral convolution

In order to visualize the B field orientation on other intensity maps, such as *Planck* or *Herschel* emission maps, we use the line integral convolution (LIC; Cabral & Leedom 1993) filtering technique. The method filters ('blurs') an input image texture along local vector field lines, in our case showing the orientation of the magnetic field lines.

When applying the LIC algorithm based on *Planck* information at 10 arcmin on the 250 μm *Herschel* map at $\sim$20 arcsec resolution, we make the assumption that the orientation of the B field is not changing inside the *Planck* beam. This is a strong assumption which ignores any kind of small-scale patterns, which could come for example from turbulence. Hence, this process is valid only when comparing large-scale features.

3.2 Rolling Hough transform

Several different methods have been used for identifying linear structures and quantifying their orientation. For example, Peretto et al. (2012) and Palmeirim et al. (2013) used the DisPerSE method (Sousbie 2011) to extract the crests of linear structures, and calculated their average orientations. Other methods include column density gradients (Soler et al. 2013; Planck Collaboration XXXV 2016), inertia matrix (Hennebelle 2013), and Hessian matrix (Planck Collaboration XXXII 2016).

As our interest here is mostly in diffuse striations, we use the Rolling Hough transform (RHT; Clark et al. 2014). The RHT is a machine vision method based on the Hough transform (Hough 1962). It calculates the intensity as a function of angle in a circular region around every pixel of image data. The RHT thus quantifies the orientation of linear structures, rather than simply identifying them. By contrast, the DisPerSE method (Sousbie 2011), originally developed for cosmic web data, defines filaments as structures that connect local density maxima. This requirement is not well suited for characterizing striations. Indeed, we find that in order for DisPerSE to locate the faintest striations, the persistence threshold must be set so low that many spurious structures were also returned. Even then, the RHT-defined structures are a better representation of the striations seen by eye.

We quantify the orientations of linear structures, and the orientation uncertainties, from the RHT output using the equations defined in Clark et al. (2015). The RHT approach enables a direct pixel-by-pixel comparison of the structure orientation with the magnetic field orientation. We use the default parameter values of the RHT.

The RHT output is three-dimensional: intensity as a function of angle for every pixel in the input image. Integrating the RHT output over all possible angles produces the RHT backprojection, a visualization of the linear intensity in the image (see Clark et al. 2014, for details).

3.3 Histogram of relative orientations

Soler et al. (2013) (and Planck Collaboration XXXV 2016) use the name histogram of relative orientations (HRO) to refer to their method of using column density gradients to extract linear structures. Confusingly, they use the same name to refer to the end result, the actual histogram comparing the relative orientation of structures and magnetic field. We take the same approach as Planck Collaboration XXXVIII (2016) and use the name HRO to refer just to the histogram in general, regardless of how the orientation of the structures has been determined.

We perform an HRO analysis to quantify the alignment between the magnetic field and the *Herschel* 250 μm elongated structures traced by the RHT method. We build the angle difference between the B field orientation $\theta_{\rm B}$ and the structure orientation $\theta_{\rm RHT}$ in each pixel by

$$\Delta\theta = \theta_{\rm B} - \theta_{\rm RHT}\,. \tag{6}$$

This angle difference is only computed where the uncertainty of the B field and the RHT orientations are simultaneously below 10°.

3.4 Multivariate analysis methods for analysing HROs

We want to examine how the relative alignment of dust structure and magnetic field changes with column density. It is expected that the two are preferentially aligned in low column density environments, and perpendicular in high column densities (e.g. Planck Collaboration XXXV 2016). We want to go a step further to build a robust quantification to reveal the transition between the two modes, without any a priori knowledge on the components. This is why we use multivariate analysis methods to determine the basic ways in which the HROs vary as a function of column density.

We use a two-step method to analyse quantitatively the HROs described in the previous section. In the first step, we use a variant of principal component analysis (PCA; see e.g. Jolliffe 2002) to estimate the number of components in the HROs. PCA is a statistical method used to find the principal components of the data, i.e. the directions with the most variance. The method is often used to reduce the dimensions of the data. First, we divide the *Herschel* map into 18 continuous bins of column density, all containing the same number of pixels. The HRO analysis described above is then performed on each column density bin separately, yielding a set of 18 HROs. Then, we create the matrix M, whose columns contain the 18 HROs. We compute the principal components of matrix M using PCA. The principal components constitute a basis to the set of histograms contained in M. Since the components are orthogonal by definition, it is difficult to interpret them in physical terms (in particular because they contain negative elements). Therefore, we only use PCA to estimate the number of main components.

In the second step, we apply non-negative matrix factorization (NMF; Lee & Seung 1999) to the matrix M. NMF is a multivariate analysis technique, which is used to factorize a matrix M of dimension $(m \times n)$ into two matrices W $(m \times p)$ and H $(p \times n)$, where

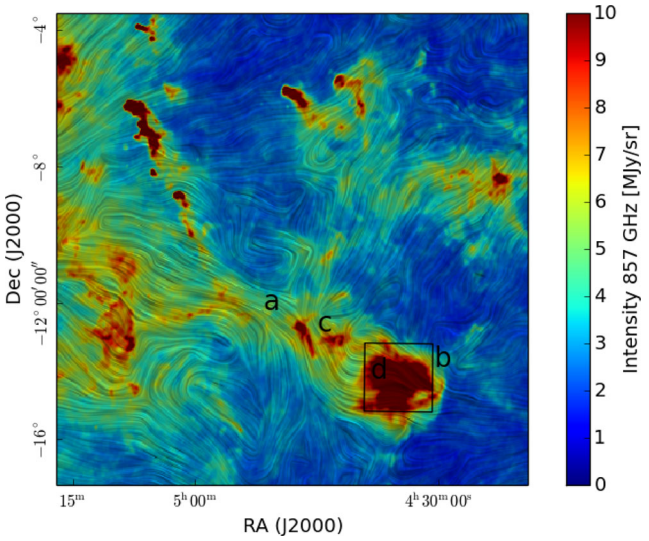

Figure 1. Region surrounding L1642 in *Planck* 857 GHz intensity map with POS magnetic field orientation shown by the LIC texture at 30 arcmin resolution (see the main text for details). Structures discussed in the text are marked with letters a–d. L1642 ($\alpha_{2000} = 4^{\rm h}35^{\rm m}$ and $\delta_{2000} = -14^\circ 15'$) is located at the SW corner of the image (marked with a square), at the head of an over 5°-long H I pillar oriented towards NE. There are also two smaller dense blobs at the centre of the pillar, at approximately $\alpha_{2000} = 4^{\rm h}45^{\rm m}$, marked with 'c'. The details of the figure are best seen in the electronic version.

p is usually notably lower than m or n. All the matrices can have only non-negative elements. Usually, the problem must be approximated numerically forming $V = W \times H + U$, where U is a residual matrix. The dimensions of W and H must be defined. m is defined by the number of rows in M, i.e. the number of different angle bins in our case. n is defined by the number of columns in M, i.e. the number of HROs ($n = 18$) in our case, while p, the number of rows in H, or elementary histograms we wish to extract, must be set by the user. We use the number of the main components in M obtained with PCA in step 1. The algorithm to compute W and H was presented in Lee & Seung (1999). It is initialized with random W and H matrices, and it uses iterative update rules to minimize the Euclidian distance between M and $W \times H$. It should be noted that NMF is similar in many regards to "positive matrix factorization' (PMF), introduced by Paatero & Tapper (1994), which differs mainly in terms of optimization algorithm. Both NMF and PMF have been applied in astronomy (see, e.g., Juvela, Lehtinen & Paatero 1996; Berné et al. 2007).

The solution to NMF is not unique and can depend on the initialization; hence, we run NMF 1000 times on M to empirically verify that the solution is constant in our specific case. The resulting components in H extracted by NMF are elementary histograms. The NMF method produces directly the weights contained in W, i.e. the contribution of each component to the histograms of M, which can then be shown as a function of the column density. This analysis is performed in Section 4.5.

4 RESULTS

4.1 *Planck* polarization and magnetic field orientation

The *Planck* 857 GHz intensity map with POS magnetic field orientation of the area surrounding L1642 is shown in Fig. 1. L1642 is located at the head of a large, over 5°-long pillar structure visible in H I and infrared/submillimetre dust emission maps. We use the LIC method described in Section 3.1 to visualize the POS magnetic field. The magnetic field orientation is shown at 30 arcmin resolution, since, at full resolution, the S/N of the polarization data in the surrounding low column density region is low, as there is not much material to emit polarized radiation. We use equatorial coordinates and refer to directions north (N, up), south (S, down), east (E, left), and west (W, right) in this and all other images.

The large-scale POS magnetic field in Fig. 1 shows a lot of turmoil in this region. The areas discussed below are marked with letters a–d in the figure. The large pillar leading to L1642 appears to be a turning point to the large-scale magnetic fields. On the E part of the pillar (a), the magnetic field is oriented approximately midway between the E-W and NE-SW directions. On the NW side of L1642 (b) the B field is oriented in the NW-SE direction, that is approximately perpendicular to the E side. In the centre of the pillar (c), where there are two dense, elongated structures, these perpendicular B fields meet and the field lines bend. However, at the W part of the pillar and at the head where L1642 is situated (d), the B field is again at E-W orientation. Thus, the NW part of L1642 faces again a perpendicular B field. The impact of the surrounding region to the L1642 cloud is discussed more in Section 5.

Fig. 2 shows maps of the *Planck* 353 GHz intensity I, polarization angle dispersion function S, the MAS estimate of polarization fraction $p_{\rm MAS}$, magnetic field orientation angle $\theta_{\rm B}$, S/N of the $p_{\rm MAS}$, and the dispersion of the orientation angle $\sigma(\theta_{\rm B})$ of the L1642 cloud, all at 10 arcmin resolution. The magnetic field orientation $\theta_{\rm B}$ shows a sharp transition between the NW and SE regions, as the B field orientation changes abruptly near the densest part of L1642.

The polarization fraction $p_{\rm MAS}$ is very low at the densest parts of the cloud. The polarization fraction is high only in the N part of L1642, where striations are more visible. There is clear anticorrelation between S and $p_{\rm MAS}$. In the N area of the striations, the S level is low, and $p_{\rm MAS}$ relatively high, which is consistent with a well-ordered magnetic field in this part. As shown in the *Planck* observations overview (Planck Collaboration XIX 2015) and related simulations (Planck Collaboration XX 2015), variations of the B field direction within the beam or along the line of sight (e.g. due to tangling) would result in a decrease of the observed polarization fraction. The relatively high value of $p_{\rm MAS}$, coinciding with a low S level, indicates that the field is uniform in this area.

4.2 Structures in *Herschel* submm maps

Malinen et al. (2014) examined the general structure and star formation activity of molecular cloud L1642 using especially *Herschel* dust emission maps. Their data showed differences in the different parts of the cloud. In this paper, we continue with a more detailed analysis of the cloud structure. Fig. 3 (left) shows the *Herschel* column density map with named regions A, B, C, and D. Although the cloud is shaped more like a blob than a filamentary structure, it contains several elongated features. As noted in Malinen et al. (2014), there are clear striations in the diffuse cloud surrounding the star-forming, dense area, e.g. in the N side of the cloud (S1 in the figure). There are also interesting structures that may fall between the concepts of 'filament' and 'striation', for example the spiralling 'tail' in the east (S2 in the figure). There are also striations directly connected to the main parts of the cloud, especially in the W part, where they form part of the A structure (S3). All these striations have column densities of typically $N_{\rm H} < 2 \times 10^{21}$ cm^{-2}. Also, the two elongated, straight structures (S4) between regions B and C are

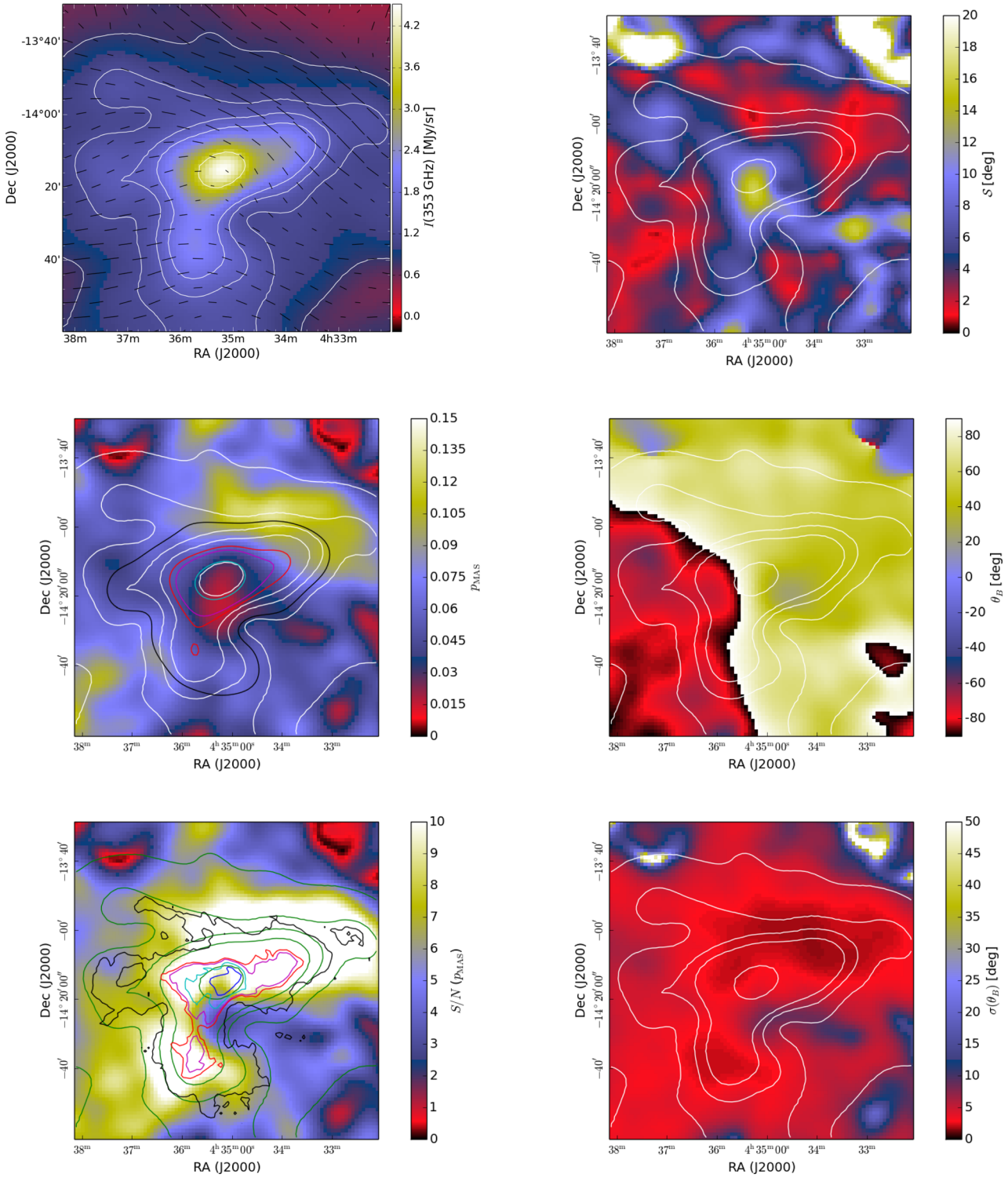

Figure 2. *Planck* 353 GHz intensity, polarization angle dispersion function S, MAS estimate of polarization fraction $p_{\rm MAS}$, magnetic field orientation angle $\theta_{\rm B}$, S/N of $p_{\rm MAS}$, and $\sigma(\theta_{\rm B})$ maps at 10 arcmin resolution. The white (and green) contours are from the *Planck* 353 GHz intensity map. *B* field is visualized with vectors on the intensity map. The blue, cyan, magenta, red, and black contours on the $p_{\rm MAS}$ and S/N of $p_{\rm MAS}$ maps show the column density based on *Herschel* data at 5.22, 3.0, 2.0, 1.74, and 1.0 $\times$ 10^{21} cm^{-2}, respectively. The *Herschel* data are shown at 10 arcmin resolution (on the $p_{\rm MAS}$ map) and at the original 40 arcsec resolution (on the S/N of $p_{\rm MAS}$ map). The highest (blue) contour is not seen at 10 arcmin resolution.

not typical filaments or striations. S5 marks another linear feature almost perpendicular to the S4 structures.

The previously known objects, including three young stellar objects (YSOs) binary B-1, binary B-2, and B-3, and a cold clump B-4, inside the densest cloud (Malinen et al. 2014), together with the submillimetre clumps from Montillaud et al. (2015) have been marked in Fig. 3 (right). Galaxies and non-reliable objects have been removed from the list. In the densest

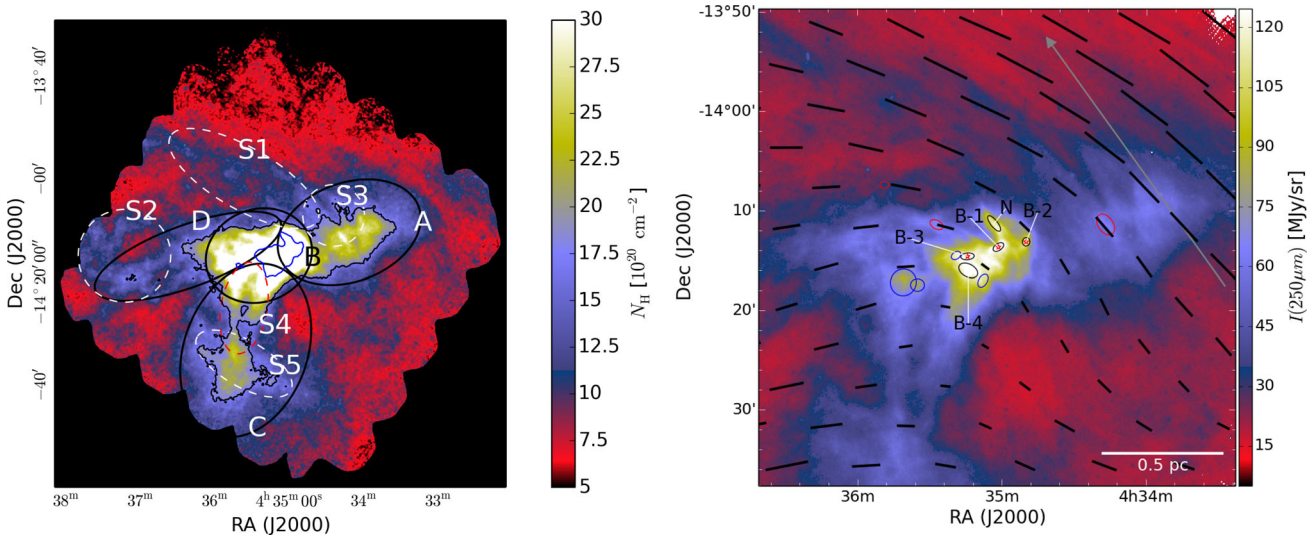

Figure 3. Left: *Herschel* column density map with regions A, B, C, and D, and contours at 1.74×10^{21} and 5.22×10^{21} cm^{-2} used for RHT analysis (see the text for details). Other structures discussed in the text are marked with dashed white (or red) ellipses. S1, S2, and S3 mark striations, S4 marks elongated structures between regions B and C, and S5 marks another linear feature almost perpendicular to the S4 structures. Right: *Herschel* 250 μm intensity map with sources from Malinen et al. (2014): YSOs B-1, B-2, and B-3, cold clump B-4, and an elongated structure N marked with black ellipses. The YSOs are also marked with red stars. Bound and unbound submillimetre clumps from Montillaud et al. (2015) are marked with blue and red ellipses, respectively. *B* field is visualized with vectors. The grey arrow shows the location of the cut used in the CO analysis in Fig. 11.

central part of the cloud, there is also an elongated extension, resembling a finger (marked N in the figure), towards north. This type of structure would not usually be considered filament or striation.

To extract structures in the *Herschel* map, we use the RHT method (described in Section 3.2). We analysed the RHT results separately for the whole area and for selected regions. We used the column density N_H map to define a threshold in column density to separate diffuse ($N_H < 1.74 \times 10^{21}$ cm^{-2}) and dense ($N_H > 1.74 \times 10^{21}$ cm^{-2}) regions. We then divided the dense medium into four regions: A, B, C, and D. The region B is defined as the region of highest column density, $N_H > 5.22 \times 10^{21}$ cm^{-2}, shown in Fig. 3 (left) with a contour. The other regions are defined as belonging to the respective ellipse shown in Fig. 3 (left), and having column density values 1.74×10^{21} cm^{-2} $< N_H <$ 5.22×10^{21} cm^{-2}.

Fig. 4 shows the linear structures extracted with the RHT method, and the reliability of the detections. The results match the structures seen in the map very well, revealing detailed, linear structures both in the diffuse regions and in the denser parts of the cloud. We note that in addition to these, the RHT map shows two structures resembling the body of a fishbone, with linear 'spine' and approximately perpendicular 'bones', marked in the Fig. 4 (top). The reliability map does not show notable difference in the structures between diffuse and dense regions.

4.3 Visual comparison of *Planck* and *Herschel* data

Fig. 3 (right) shows the magnetic field lines derived from *Planck* polarization map (at 10 arcmin resolution) plotted with vectors on the *Herschel* 250 μm intensity map (at ∼18.3 arcsec resolution) of the cloud L1642. The lengths of the vectors are proportional to the polarization fraction. For comparison, Fig. 5 shows the *B* fields with an LIC map (described in Section 3.1). There are clear differences in the magnetic field orientations in the different areas of the cloud. In the NW part of the cloud, the magnetic field lines are oriented between NE-SW. In the S and E parts of the cloud, the lines are oriented mostly between E-W. However, when the lines reach the W point of the dense region, they turn abruptly approximately 90°, almost towards S, along with the lines in the W part. Similarly, when the lines at the E and N regions meet at NE at the outskirts of the cloud, they turn towards the same orientation, almost to S. The densest part of the cloud is exactly where the *B* field is bending the most.

The eastern, filamentary curving tail (S2) of the cloud is located in the area where *B* field lines with different orientations meet. The orientation of the two linear structures (S4) between the regions B and C differs by ∼30°. As the field lines curve in this region, both structures are in fact approximately perpendicular to the local magnetic field. The largest elongated structure (N) of the main cloud pointing towards NE is approximately aligned with the magnetic field. Some of the structures extracted by the RHT method, especially in region A and west of region B, resemble fishbones, with an elongated structure as the spine, and perpendicular smaller structures or striations on both sides. Comparing to the LIC texture, these structures are not exactly perpendicular or aligned with the magnetic field, but could be moving and evolving. Especially region A looks as if it is bend and shaped by the magnetic field. The roundish general structure is revealed to be formed of thin slices when looked in more detail. Comparing the magnetic field lines to the *Herschel* map, it is evident how well the field lines follow the general structure of the cloud even to the finer details, and the diffuse striations surrounding the cloud.

4.4 Polarization fraction versus column density

Fig. 6 shows the polarization fraction p_{MAS} as a function of the column density (derived from *Herschel* maps), for data at 10 arcmin resolution. The sample points are taken every 5 arcmin. The polarization fraction is notably reduced above $N_H = 2 \times 10^{21}$ cm^{-2}. The upper envelope of the polarization fraction distribution begins to decrease already below this column density value. Reduced polarization fraction is observed over a large area where the magnetic field orientation is still mainly uniform (see Fig. 2). For comparison,

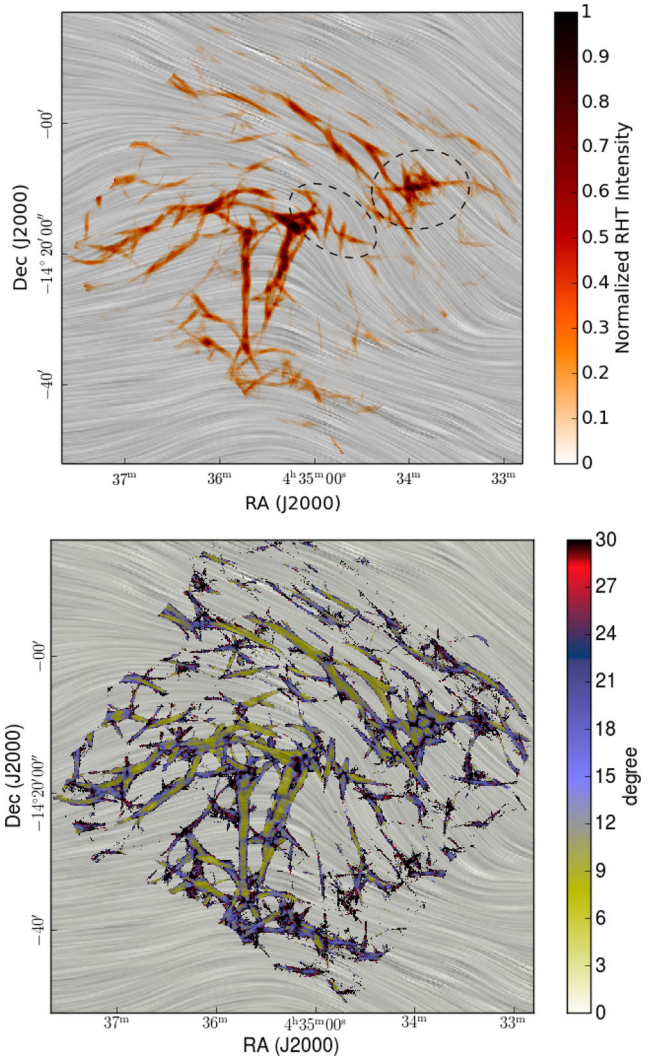

Figure 4. Top: structures extracted by RHT analysis of *Herschel* 250 μm map. The ellipses show two structures resembling a fishbone with 'spine' and approximately perpendicular 'bones'. Bottom: uncertainty of the RHT orientation angle $\theta_{\rm RHT}$. The HRO analysis is restricted to regions where the uncertainty is below 10°. The grey background shows the POS magnetic field orientation with LIC texture.

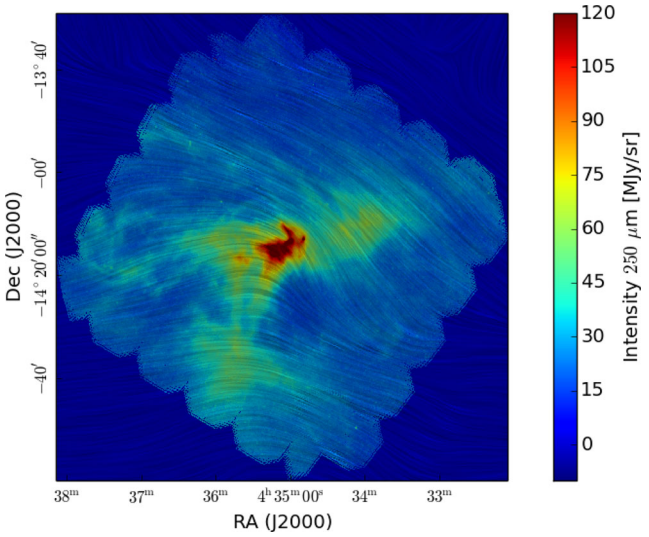

Figure 5. L1642 in *Herschel* 250 μm map (at 18.3 arcsec resolution) with *Planck* magnetic field orientation (at 10 arcmin resolution) visualized by LIC texture. The details of the figure are best seen in the electronic version.

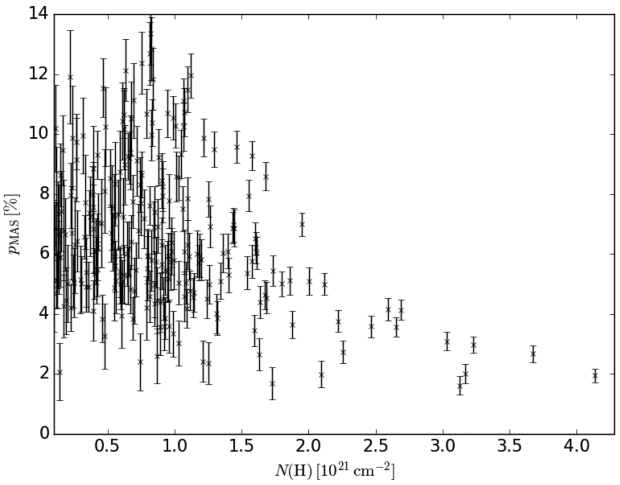

Figure 6. Polarization degree $p_{\rm MAS}$ (based on *Planck* data) as a function of the column density (based on *Herschel* data). The data are at a resolution of 10 arcmin, and the samples are taken every 5 arcmin.

the middle-left frame of Fig. 2 shows the column density contours (at 10 arcmin resolution) on the $p_{\rm MAS}$ map. Although most of the high column density pixels originate in the central region B, also region A has a significant number of pixels above $N_{\rm H} = 2 \times 10^{21}$ cm^{-2}. All of the highest column density pixels $N_{\rm H} > 3 \times 10^{21}$ cm^{-2} originate in the central region B within a few *Planck* resolution elements. The high column density points in Fig. 6 are therefore highly correlated and come from a relatively small area.

Part of the depolarization (and most of the scatter) could be related to changes in magnetic field orientation, either at small scales not resolved by *Planck* or in regions along the line of sight where POS orientation of the magnetic field differs. However, it is possible that the column density dependence is caused by a partial loss of grain alignment in the densest parts of the cloud. If grain alignment is assumed to be caused by radiative torques (see review by Lazarian 2007), the change would be directly related to the attenuation of the radiation field. This increases the lower size limit of the dust grains that remain aligned in the magnetic field. Thus, Fig. 6 could point to an almost complete loss of grain alignment in the cloud centre, and the minimum values of $p_{\rm MAS}$ could be attributed to polarized emission from diffuse regions along the line of sight.

The column density dependence of the polarization fraction has been discussed in the recent *Planck* papers (Planck Collaboration XIX 2015; Planck Collaboration XX 2015; Planck Collaboration XXXIII 2016). Planck Collaboration XIX (2015) concluded that the general decrease of p with $N_{\rm H}$, at the resolution of 1°, was mainly due to fluctuations in the B field orientation along the line of sight, probing various components in particular towards regions close to the Galactic plane. This was supported by the anticorrelation observed between p and S. In our case of a high-latitude cloud, there is not as much confusion along the LOS. However, we see an increase of S towards the central part associated with the highest $N_{\rm H}$ values. In this paper, we are only looking at one cloud and not making a statistical analysis of several regions. Therefore, it is not clear what is the cause of the decrease of p in our particular case.

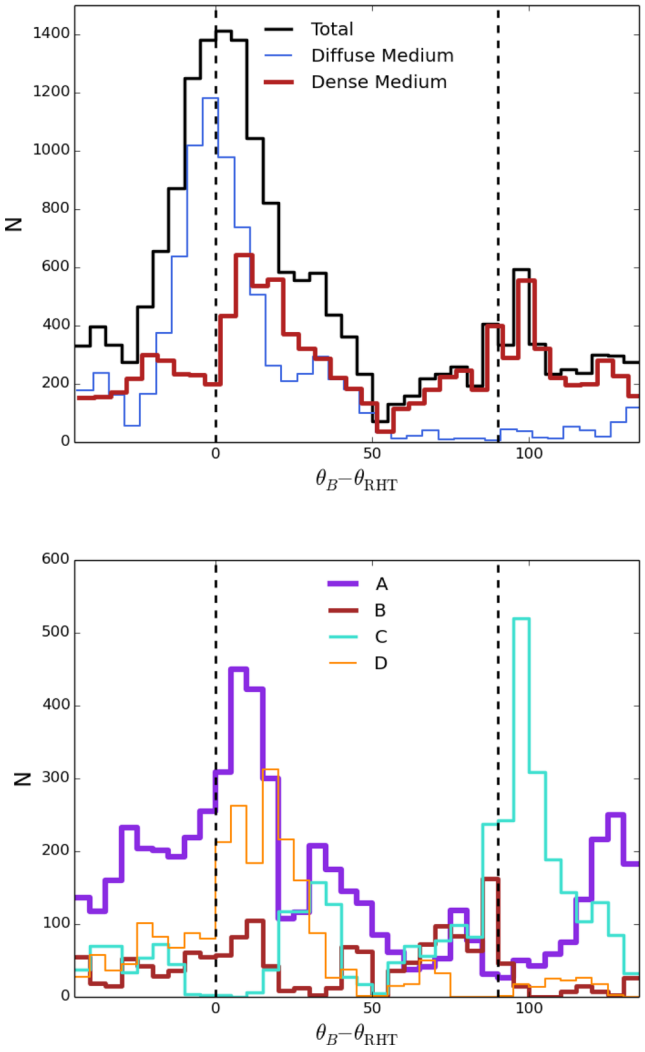

Figure 7. HRO analysis comparing the relative orientation of magnetic field and cloud structure in the case of the whole data or dense and diffuse areas (top), and in the case of separate regions defined in the main text and shown in Fig. 3 (left). *N* gives the number of pixels. Vertical dashed lines show the values 0° and 90°. The lines for dense and diffuse areas in the (top) figure are shifted slightly to the right.

4.5 Relative orientation of magnetic fields and *Herschel* structures

4.5.1 Relative orientation in different regions

We perform an HRO analysis (as described in Section 3.3) to quantify the alignment between the magnetic field and the *Herschel* 250 μm elongated structures traced by the RHT method. The resulting histograms are shown in the top frame of Fig. 7 for the entire region, and split between the diffuse and dense regions. There are two peaks in this distribution, approximately centred at 0° and 90°. The HRO computed on the diffuse regions is mainly associated with the first peak at 0°, while the HRO of the denser regions is more complex.

When splitting the denser areas into four physical regions, A, B, C, and D (as defined in Section 4.2), it appears that the structures in C are clearly perpendicular to the magnetic field, while the A and D regions have structures mainly aligned with the magnetic field (see Fig. 7, lower frame). In the densest region B, there is no clear distinction anymore. This is mainly due to the fact that the distribution of the RHT angles (tracing the matter) is much more flat because of confusion along the line of sight. Fig. 2 shows that the orientation of the magnetic field is reliable and very uniform in the full region. We also note that the distribution peaks are not exactly at 0° and 90°, but slightly above those values. Region A also shows another, smaller peak at ∼130°. The 'fishbone'-like structures shown in Fig. 4 (top) are in the A region, and are likely to contain most of the pixels causing this peak.

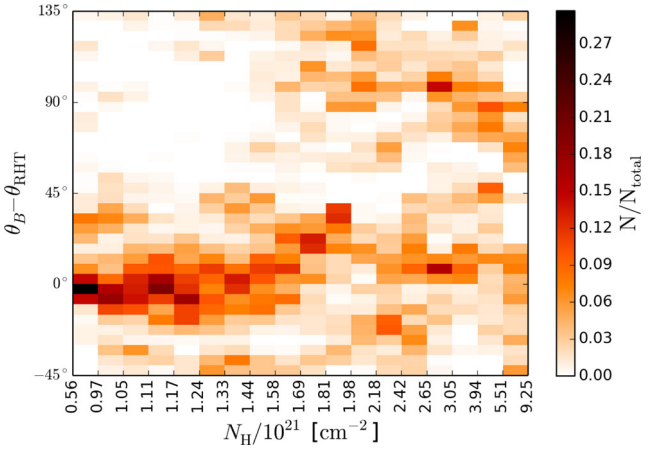

Figure 8. The elementary histograms of angle difference built per bin of column density, so that all histograms contain the same number of pixels. Each histogram is normalized by its integral.

4.5.2 Column density dependence of relative orientation

We analyse the column density dependence of relative orientation using the method described in Section 3.4. We have divided the *Herschel* map into 18 continuous bins of column density between 0.56×10^{21} and 9.25×10^{21} cm^{-2}, all containing the same number of pixels. The HRO analysis described above is then performed on each column density bin separately, yielding a set of 18 HROs, which are combined in matrix *M*, and shown in Fig. 8. We run an initial PCA analysis on this set, and find that 95 per cent of the power in *M* can be expressed with the first two components.

In the second step, we apply NMF to factorize matrix *M* into the product $W \times H$, where the dimensions of *H* are $(p \times n)$, and $n = 18$. As we have seen above in the PCA analysis, the data are contained in a dimension 2 subspace and hence we can apply NMF directly with $p = 2$. We then run NMF 1000 times on *M* to empirically verify that the solution is constant. The two final averaged components found in the Monte Carlo runs are shown in Fig. 9. As expected, one component has a clear peak at 0°, while the other component has two main peaks, near 0° and 90°.

The weights contained in *W*, i.e. the contribution of each component to the 18 histograms of *M*, are shown as a function of the column density in Fig. 10. This confirms that one component is associated with diffuse regions and one with dense regions. We see a clear transition around a column density at $N_{\rm H} \sim 1.6 \times 10^{21}$ cm^{-2}. Planck Collaboration XXXV (2016) derived a threshold value of $N_{\rm H} = 10^{21.7} \sim 5 \times 10^{21}$ cm^{-2} in their analysis, but using another convention for the dust opacity κ. To compare with our estimate, we need to divide their value by 3 leading to $N_{\rm H} \sim 1.67 \times 10^{21}$ cm^{-2}, which is in good agreement with our result. The other way, our estimate corresponds to $N_{\rm H} \sim 4.8 \times 10^{21} \sim 10^{21.7}$ cm^{-2} using their convention for κ.

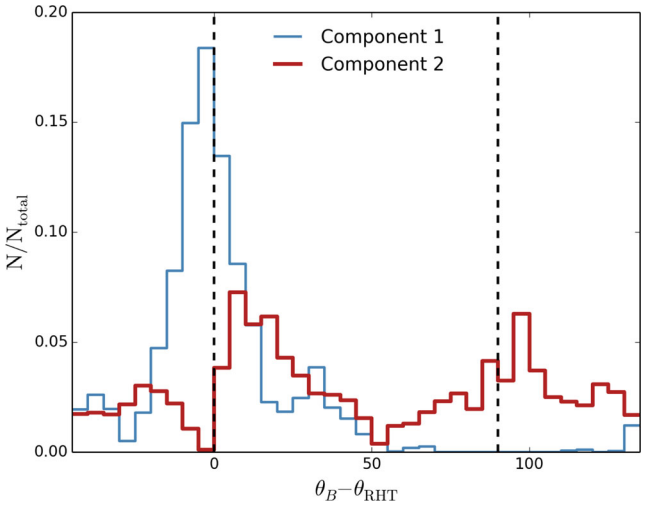

Figure 9. The two principal components found with the NMF algorithm applied on the 18 histograms of angle difference built per column density bin. The horizontal axis shows the relative orientation of magnetic field and cloud structure. Each component is normalized by its integral.

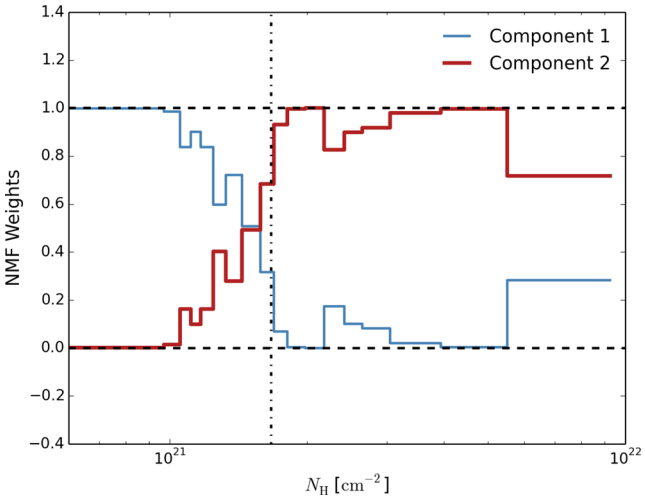

Figure 10. The weights of the components in NMF analysis, i.e. the contribution of each component to the 18 histograms as a function of column density. The image shows the transition where the relative orientation of density structures and magnetic field lines changes from preferentially aligned to perpendicular. The dashed vertical line shows the similar result obtained by Planck Collaboration XXXV (2016), see the main text for details.

4.6 Comparison to CO

We use the CO data presented and analysed by Russeil et al. (2003) to compare with the *Herschel* map and magnetic field orientations in terms of morphology and kinematics. The general morphology of the cloud revealed by the CO data is very similar to the *Herschel* data shown in Fig. 3 (left). It is dominated by the bright clumps A, B, and C (Fig. 11a). The eastern parts of the main filamentary structures in the north (S1) and east (S2) of L1642 are also visible. The western parts of these structures are overwhelmed by the emission of the main cloud and can be partly revealed when selecting the larger velocities (Fig. 11b). However, the relatively low resolution of the CO data does not enable us to resolve the striations in these structures, similarly to *Planck* data.

The large-scale kinematics was studied by Russeil et al. (2003). Their figure A.1 shows channel maps of ^{12}CO(1–0). One part of the cloud, including most of the central (B) and south (C) parts of the cloud, has velocities mainly between $V_{\rm LSR} = -0.1$ and 0.5 km s^{-1}, while another part, including mostly the west (A) and north regions of the cloud, has velocities between $V_{\rm LSR} = 0.7$ and 1.5 km s^{-1}. The north and east filamentary structures (S1 and S2) are connected to this second, more redshifted, structure. In Fig. 11(c), we show the map of peak velocity obtained by a Gaussian fit of the ^{12}CO(1–0) line.

Interestingly, at $V_{\rm LSR} > 1$ km s^{-1}, the emission of all CO transitions is dominated by the northern part of clump A, at the root of the striations of the northern structure S1 (Fig. 11b). Fig. 11(d) shows the position–velocity (PV) diagram in ^{12}CO(2–1) along a cut through clump A (grey arrows in Fig. 11). We find a velocity gradient of ∼1 km s^{-1} over the ∼15 arcmin (0.6 pc) width of clump A (between offsets of 5 and 20 arcmin). The velocity then tends to stabilize around 1.1 km s^{-1} when penetrating the striation region, on the western edge of S1 (offsets > 20 arcmin). The cut is shown also on the *Herschel* map in Fig. 3 (right), revealing that it goes through the western head of clump A, and parallel to the striations (S3) on the northern part of clump A. For comparison, we also made a slightly different cut, aligned with the striations of S3 and the B lines. This does not notably change the properties of the PV cut.

5 DISCUSSION

5.1 Connection between magnetic fields and cloud structure

L1642 is one of the Orion outlying clouds located at the head of a long H I pillar structure. The cloud itself is elongated in the equatorial E-W direction, forming a complex, partly cometary-shaped structure. As shown in Malinen et al. (2014), there are three cores with YSO systems (two binary and one single) with approximately equal distances between the cores, along a straight line, and apparently in age order from the youngest one (B-2) in the west to the oldest (B-3) in the east. For a cloud with such low mass (∼72 M$_\odot$) and high latitude, L1642 has unusually high star formation efficiency, ∼7 per cent (Malinen et al. 2014).

The *Planck* polarization data shown in Figs 3 (right) and 5 reveal an ordered magnetic field that pervades the cloud from NE to S. In the smallest scales of the *Herschel* map, magnetic field is nearly perpendicular to the line connecting the YSOs, at least at the western part of the dense region B. The magnetic field orientation is also closely correlated with the diffuse material surrounding the cloud, as the low-density striations are aligned with the magnetic field orientation. There clearly is a complex interplay between the cloud structure and large-scale magnetic fields revealed by *Planck* polarization data. This suggests that the large-scale magnetic field is closely linked to the formation and evolution of the cloud. However, it is an open question whether magnetic fields shape the cloud, or if the cloud material shapes the magnetic field, or if they both are simultaneously affected by some physical force.

Already Taylor, Taylor & Vaile (1982) predicted that a shearing flow of material is shaping the cloud. Malinen et al. (2014) discussed the connections between L1642 and its larger surroundings. To summarize, L1642 appears to be affected mostly by a flow coming from the NW/W, or the cloud itself is travelling to NW/W. Both the large-scale (Fig. 1) and the smaller scale (Fig. 5) LIC maps show bending magnetic fields at the NW side of L1642, corresponding to the findings of Malinen et al. (2014) that the cloud seems to be affected by a compressing force from the NW direction. The

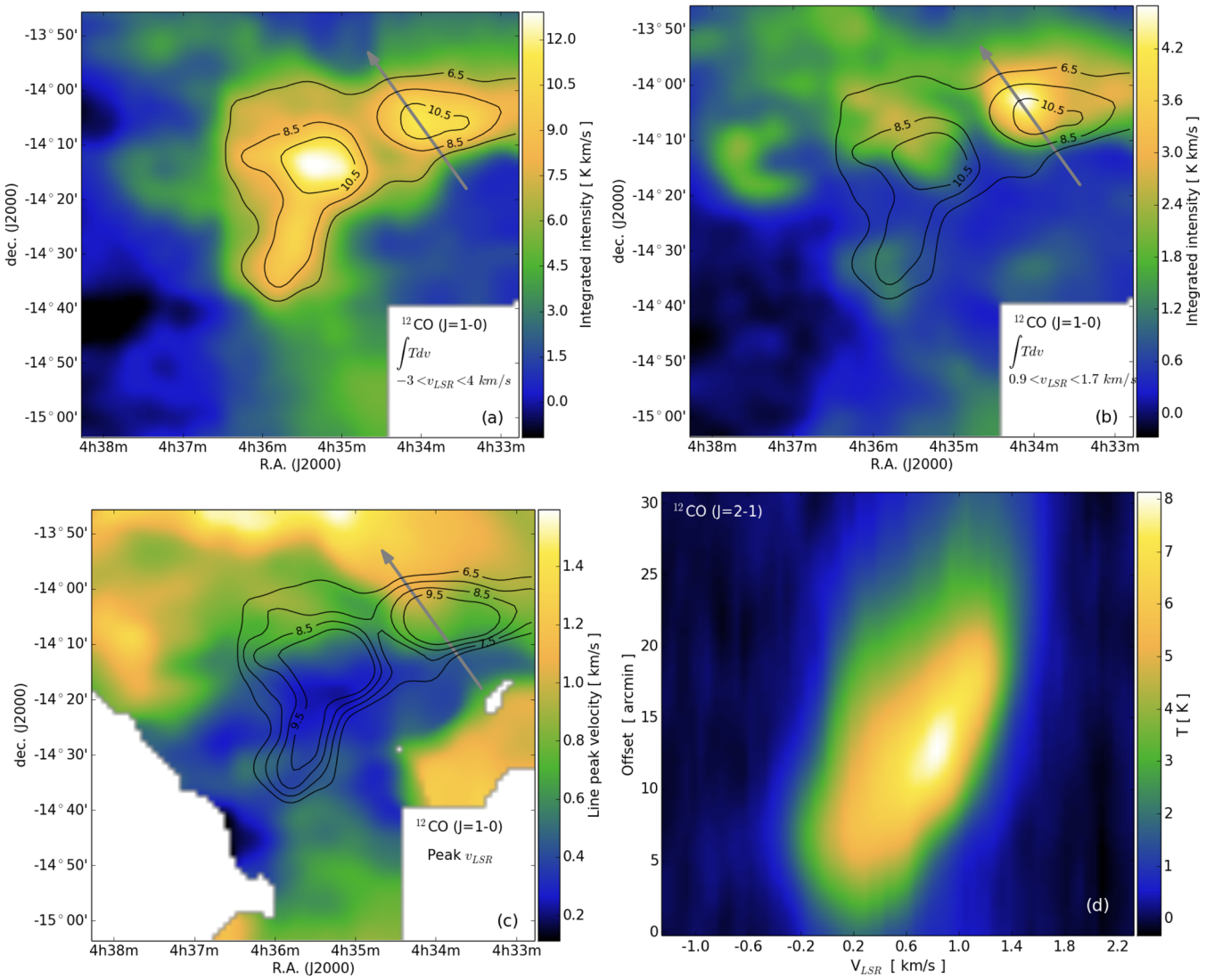

Figure 11. ^{12}CO data of L1642, based on the observations of Russeil et al. (2003). (a) Total integrated intensity, (b) intensity integrated within $0.9 < v_{\rm LSR} < 1.7$ km s^{-1}, (c) peak velocity obtained by a Gaussian fit of the ^{12}CO(1–0) line, (d) position–velocity diagram of ^{12}CO(2–1) along a cut through clump A and a striation. The cut is shown with grey arrow in the other figures. $v_{\rm LSR}$ is the radial velocity relative to the local standard-of-rest (LSR) frame. Here, T is the antenna temperature, i.e. it represents the intensity of the emission. The black contours show the total integrated intensity.

cloud morphology and the apparent compression that is shaping the cloud from the west suggest that star formation in L1642 may be externally triggered. The open question is, what is causing the force shaping the cloud and bending the magnetic field? Lee & Chen (2009) studied star formation in a group of clouds (not including L1642) around the Orion–Eridanus Superbubble, and concluded that compression from the superbubble can potentially have a long-range triggering influence causing star formation in affected clouds. L1642 is located between two large bubbles, the Orion–Eridanus Superbubble and the Local Bubble (see Alcalá, Covino & Leccia 2008; Malinen et al. 2014, for a summary). It is possible that this extreme location is enough to cause the observed phenomena and be the trigger of star formation in this cloud.

This study clearly shows the connection between the large-scale magnetic field and small-scale cloud structure in L1642. However, the conditions affecting the cloud could mean that magnetic field has more effect here than in other regions. Also, the geometry of this object can be favourable to reveal such features, as it is quite isolated, in high latitude, and shows clear magnetic field orientation. Statistical studies comparing other regions combining *Planck* and *Herschel* data would be useful to determine how common these features are. Also, high-resolution polarization observations would reveal more details of the small-scale connections between density structures and magnetic fields.

5.2 Dynamics of the cloud and its striations

In Section 4.6, we reported the detection of a clear velocity gradient through clump A with a continuous variation in velocity from the south edge of clump A to the north-east, parallel to the close-by striation (S3). Since the angle between the striation and the POS remains unknown, it is unclear whether the redshifted gas is approaching clump A or escaping from it.

One possibility is that gas is photoevaporating from clump A due to the surrounding interstellar radiation field. However, the dust temperature determined from *Herschel* data in this part of the cloud,

∼15–16 K (Malinen et al. 2014; Montillaud et al. 2015), does not support the idea of UV-rich region, and no ionizing star is known in the vicinity of L1642. On the other hand, the gas may well be much hotter than dust at the diffuse cloud surface. Assuming 100 K gas temperature, the sound speed is ∼1 km s^{-1}. In this simplified case, the gas would flow outwards approximately a few times 0.1 pc in time-scales of a few 10^5 years, which is compatible with the extent of the striations and the typical lifetime of molecular clouds.

Alternatively, the gas north of clump A could be infalling into clump A along the striations and following the magnetic field lines. In Russeil et al. (2003), the total mass of the cloud was estimated to be ∼60 $M_\odot$ based on the CO data. In Malinen et al. (2014), the total mass was estimated to be slightly higher, ∼72.1 $M_\odot$, based on dust emission. If one assumes accretion on to a 10 $M_\odot$ clump, the free-fall velocity at the distance of 5 arcmin should be ∼0.7 km s^{-1}. This value would be in good agreement with the observed difference in velocity between the centre of clump A and the striations if one assumes that the angle between the striations and the POS is not too small. However, the relevance of this assumption is not clear, and the observed velocity difference could be too large to be due solely to infall.

Rotation of clump A around an axis in almost east–west orientation and almost in the POS is another possible component in the dynamics of the cloud. If the gas were in a Keplerian orbit with a mass of 10 $M_\odot$ and a radius of 0.2 pc, the velocity would be ∼0.5 km s^{-1}. Therefore, the combination of infall and rotation could explain the observed velocity gradient.

A last alternative we consider here is the collision between two gas streams. We mentioned in Section 4.6 that L1642 presents two structures with separated velocity ranges, the most blueshifted including the densest part of the cloud (clump B) and the southern part (clump C), while the redshifted part includes the north and west regions (including clump A), as well as the two filamentary structures S1 (north, connected to clump A) and S2 (east, connected to clump B). This scenario offers the advantage of a complete and consistent view of the evolution, morphology, and kinematics of the cloud. The cloud would originate from the material of the two flows jammed at their meeting point, and would naturally be cometary shaped. The redshifted structure would correspond to one stream that is flowing around the north edge of the blueshifted structure. The striations and the velocity gradient observed in Fig. 11 would originate from the shearing between the two streams, and would be interpreted as a flow of gas away from clump A. This would fit into the notion of Malinen et al. (2014) that clump A appears to be compressed from the SW, as the striations (S3) are seen only on the northern side of the clump. The alignment between the striations and the magnetic field lines would also originate from the shearing, assuming that magnetic field lines are frozen in the gas. Finally, this would also explain the unusually high star formation efficiency of the cloud (Malinen et al. 2014), considering its low mass and high latitude.

6 CONCLUSIONS

We have compared the large-scale magnetic field revealed by *Planck* polarization maps and *Herschel* submm dust emission maps in the high-latitude cloud L1642. We conclude the following.

(i) There is a close connection between the cloud structure and the large-scale magnetic field in L1642 and the surrounding region, suggesting that magnetic field is closely linked to the formation and evolution of the cloud.

(ii) The connection between cloud structure and large-scale magnetic field is seen even at the finest details of the cloud, most notably in the striations.

(iii) The distribution of relative orientation between cloud structure and magnetic field lines in diffuse medium has one peak centred at ∼0°, indicating that diffuse striations and B field are clearly aligned.

(iv) Dense medium presents a bimodal distribution of relative orientation centred at ∼0° and 90°, but separate regions have different behaviours: the dense south part (C) is perpendicular to the B field, west (A) and north (D) exhibit structures aligned on the B field, and in the densest region (B), we cannot make any distinction on the orientation.

(v) There is a clear transition from aligned to perpendicular structures approximately at a column density of $N_{\rm H} = 1.6 \times 10^{21}$ cm^{-2} [this equals ∼$10^{21.7}$ cm^{-2} when using the same convention for dust opacity as Planck Collaboration XXXV (2016)].

(vi) Comparison to large-scale *Planck* polarization data at ∼10 arcmin resolution is very useful even when looking at the finest structures in higher resolution data, e.g. *Herschel* at ∼18.3 arcsec.

(vii) CO rotational emission confirms that the striations are connected with the main clumps and likely to contain material either infalling to or flowing out of the clumps.

(viii) RHT, which was developed to extract linear features in large-scale diffuse H I regions, is a very useful and practical method also when studying denser regions with more complex structure.

ACKNOWLEDGEMENTS

We thank the referee for useful comments which improved the paper. We also thank Kimmo Lehtinen and Delphine Russeil for providing us the CO data from their earlier studies. MJ acknowledges the support of the Academy of Finland grants No. 285769 and 250741. SEC was supported by a National Science Foundation Graduate Research Fellowship under grant no. DGE-11-44155. The development of *Planck* has been supported by ESA; CNES and CNRS/INSU-IN2P3-INP (France); ASI, CNR, and INAF (Italy); NASA and DoE (USA); STFC and UKSA (UK); CSIC, MICINN and JA (Spain); Tekes, AoF and CSC (Finland); DLR and MPG (Germany); CSA (Canada); DTU Space (Denmark); SER/SSO (Switzerland); RCN (Norway); SFI (Ireland); FCT/MCTES (Portugal); and PRACE (EU).

REFERENCES

Alcalá J. M., Covino E., Leccia S., 2008, in Reipurth B., ed., Handbook of Star Forming Regions, Vol. I, Orion Outlying Clouds. p. 801
André P., Di Francesco J., Ward-Thompson D., Inutsuka S.-I., Pudritz R. E., Pineda J. E., 2014, Protostars and Planets VI. Univ. Arizona Press, Tucson, p. 27
Beckwith S. V. W., Sargent A. I., Chini R. S., Guesten R., 1990, AJ, 99, 924
Bergin E. A., Tafalla M., 2007, ARA&A, 45, 339
Berné O. et al., 2007, A&A, 469, 575
Cabral B., Leedom L. C., 1993, in SIGGRAPH '93 Proceedings of the 20th Annual Conference on Computer Graphics and Interactive Techniques. Imaging vector fields using line integral convolution. ACM, New York, p. 263
Clark S. E., Peek J. E. G., Putman M. E., 2014, ApJ, 789, 82
Clark S. E., Hill J. C., Peek J. E. G., Putman M. E., Babler B. L., 2015, Phys. Rev. Lett., 115, 241302
Crutcher R. M., 2012, ARA&A, 50, 29
Crutcher R. M., Nutter D. J., Ward-Thompson D., Kirk J. M., 2004, ApJ, 600, 279

Davis L., Jr, Greenstein J. L., 1951, ApJ, 114, 206
Goldsmith P. F., Heyer M., Narayanan G., Snell R., Li D., Brunt C., 2008, ApJ, 680, 428
Hearty T., Fernández M., Alcalá J. M., Covino E., Neuhäuser R., 2000, A&A, 357, 681
Hennebelle P., 2013, A&A, 556, A153
Hildebrand R. H., 1983, QJRAS, 24, 267
Hough P. V. C., 1962, Method and Means for Recognizing Complex Patterns, US Patent 3.069.654
Jolliffe I. T., 2002, Principal Component Analysis, 2nd edn. Springer, New York
Juvela M., Lehtinen K., Paatero P., 1996, MNRAS, 280, 616
Juvela M. et al., 2012, A&A, 541, A12
Lazarian A., 2007, J. Quant. Spectrosc. Radiat. Transfer, 106, 225
Lee D. D., Seung H. S., 1999, Nature, 401, 788
Lee H.-T., Chen W. P., 2009, ApJ, 694, 1423
McGehee P. M., 2008, in Reipurth B., ed., Handbook of Star Forming Regions, Vol. II, Star Formation and Molecular Clouds at High Galactic Latitude. p. 813
McKee C. F., Ostriker E. C., 2007, ARA&A, 45, 565
Malinen J. et al., 2014, A&A, 563, A125
Montier L., Plaszczynski S., Levrier F., Tristram M., Alina D., Ristorcelli I., Bernard J.-P., 2015a, A&A, 574, A135
Montier L., Plaszczynski S., Levrier F., Tristram M., Alina D., Ristorcelli I., Bernard J.-P., Guillet V., 2015b, A&A, 574, A136
Montillaud J. et al., 2015, A&A, 584, A92
Myers P. C., Goodman A. A., 1991, ApJ, 373, 509
Paatero P., Tapper U., 1994, Environmetrics, 5, 111
Palmeirim P. et al., 2013, A&A, 550, A38
Peretto N. et al., 2012, A&A, 541, A63
Pereyra A., Magalhães A. M., 2004, ApJ, 603, 584
Pilbratt G. L. et al., 2010, A&A, 518, L1
Planck Collaboration I, 2014, A&A, 571, A1
Planck Collaboration XIX, 2015, A&A, 576, A104
Planck Collaboration XX, 2015, A&A, 576, A105
Planck Collaboration XXXII, 2016, A&A, 586, A135
Planck Collaboration XXXIII, 2016, A&A, 586, A136
Planck Collaboration XXXV, 2016, A&A, 586, A138
Planck Collaboration XXXVIII, 2016, A&A, 586, A141
Plaszczynski S., Montier L., Levrier F., Tristram M., 2014, MNRAS, 439, 4048
Russeil D., Juvela M., Lehtinen K., Mattila K., Paatero P., 2003, A&A, 409, 135
Schlafly E. F. et al., 2014, ApJ, 786, 29
Soler J. D., Hennebelle P., Martin P. G., Miville-Deschênes M.-A., Netterfield C. B., Fissel L. M., 2013, ApJ, 774, 128
Sousbie T., 2011, MNRAS, 414, 350
Taylor M. I., Taylor K. N. R., Vaile R. A., 1982, Proc. Astron. Soc. Aust., 4, 440
Vaillancourt J. E., 2007, in Miville-Deschênes M.-A., Boulanger F., eds, EAS Publ. Ser. Vol. 23, Polarized Emission from Interstellar Dust. ESA, Noordwijk, p. 147
Ward-Thompson D., Kirk J. M., Crutcher R. M., Greaves J. S., Holland W. S., André P., 2000, ApJ, 537, L135

This paper has been typeset from a TEX/LATEX file prepared by the author.